Friction

Research Article

# An extension of Hertz's formula for the stiffness of conformal spherical contacts

Alberto Betti✉, Paola Forte, Enrico Ciulli

Cite this article: Betti A, Forte P, Ciulli E. *Friction* 2026, **14**(1): 9441103. https://doi.org/10.26599/FRICT.2025.944113

**ABSTRACT:** Hertz's classical theory of contact requires the surfaces to be non-conformal. Despite of this, Hertzian formulas are often used also for conformal contacts as for instance for the evaluation of pivot stiffness in tilting pad journal bearings. In this paper, finite element simulations of conformal contacts between spherical elastic bodies are performed for different materials and geometry, in particular by varying the clearance. A first result is the introduction of a novel normalization which allows to calculate stiffness as a clearance-invariant function. Then, a novel model for stiffness is introduced. The model reduces back to Hertz's theory in the non-conformal limit. The model requires fitting of three empirical parameters which depend on the boundary conditions and on the material properties. Analytical expressions for the parameters are provided for a subset of contact problems with a simple geometry and given material properties. More general formulas for the parameters will be developed in a future work.

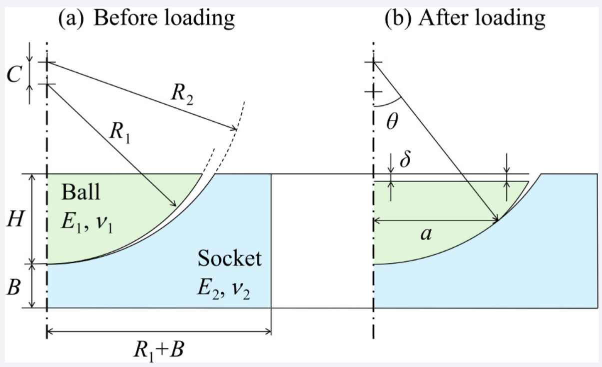


**KEYWORDS:** contact mechanics; conformal contacts; spherical contacts; stiffness model; clearance effect; Hertz's theory

## 1 Introduction

Hertz's theory for point and line contacts dates back to 1882. Under the hypothesis of frictionless contact between non-conformal, paraboloidal, elastic half-spaces, Hertz derived the equations for contact pressure ($p$), force ($F$), and area ($\mathcal{A}$) as a function of the rigid body approach ($\delta$) [1]. The research that followed aimed to relax some of the hypotheses assumed by Hertz, as reviewed by Johnson in his 1982 lecture [2]. Key contributions have been the theory of rough surfaces by Greenwood and Tripp [3] and the Johnson–Kendall–Roberts theory for surface adhesion [4]. A subset of contact problems which are not adequately described by the classical Hertz's theory is that of conformal contacting surfaces.

In conformal contacts, even for small body approaches the contact area can be relatively large, thus violating the half-space hypothesis, excluding special cases such as the plane-on-plane contact. The applications of conformal contacts are numerous, as demonstrated by previous contact mechanics studies: mechanical joints [5], artificial hips [6], spherical plain bearings [7], roller cone drill bits journal bearings [8], ball and socket pivots in tilting pad journal bearings (TPJB) [9]. While an analytical solution for the 2D conformal cylindrical contact was provided by Persson in 1964 [10], the conformal spherical contact (Fig. 1) has eluded so far an exact analytical formulation [11], which would instead be very useful indeed to avoid costly simulations, not only in industrial practice.

Given the practical importance of modelling spherical conformal contact, a number of researchers has tried to tackle such a problem through analytical or computational techniques. In 1965, Goodman and Keer [12] proposed an approximate solution for a spherical conformal contact. They simplified the analysis by assuming that the two bodies had the same elastic properties, and a Poisson's modulus of 0.25. Moreover, they assumed that the points having the same distance from the symmetry axis were paired during contact. As pointed out by Fagan and McConnachie [13], this hypothesis is not valid for contact angles larger than 25°. Goodman and Keer model produced larger contact areas and stiffer contacts, compared with Hertz's theory, in agreement with their experiments.

One of the popular analytical approaches is to approximate the socket as a Winkler's elastic foundation. In an elastic foundation, the displacement of a point depends only on the pressure in that point. This allows an analytical solution assuming a rigid ball and a soft socket. The analytical results have been compared with finite element method (FEM) results showing the limits of the developed analytical models [6, 14–19]. One debated point of Winkler's foundation models is the determination of the elastic foundation modulus. Some authors provide an analytical formula [6, 14, 15], while others recommend tuning it by using FEM

Department of Civil and Industrial Engineering, University of Pisa, Pisa 56122, Italy.

✉ Corresponding author. E-mail: alberto.betti@phd.unipi.it

Received: October 13, 2024; Revised: December 7, 2024; Accepted: March 23, 2025

**Nomenclature**

| | | | |
|---|---|---|---|
| $a$ | Radius of the contact area (mm) | $m$ | Empirical shape parameter |
| $\mathcal{A}$ | Contact area (mm²) | $p$ | Contact pressure (Pa) |
| $B$ | Socket geometrical parameter (mm) | $q_\infty$ | Intercept parameter (N) |
| $C$ | Radial clearance (mm) | $R_1$ | Ball radius (mm) |
| $d$ | Non-dimensional displacement | $R_2$ | Socket radius (mm) |
| $E_1$ | Ball Young's modulus (GPa) | $R'$ | Equivalent radius (mm) |
| $E_2$ | Socket Young's modulus (GPa) | $\delta$ | Rigid body approach (mm) |
| $E'$ | Equivalent Young's modulus (GPa) | $\delta'$ | Normalized displacement |
| $F$ | Contact force (N) | $\theta$ | Contact angle (rad) |
| $H$ | Ball geometrical parameter (mm) | $\lambda$ | Empirical shape parameter |
| $k_\infty$ | Stiffness asymptote (N/mm) | $\nu_1$ | Ball Poisson's modulus |
| $\mathcal{L}$ | Non-dimensional contact force | $\nu_2$ | Socket Poisson's modulus |

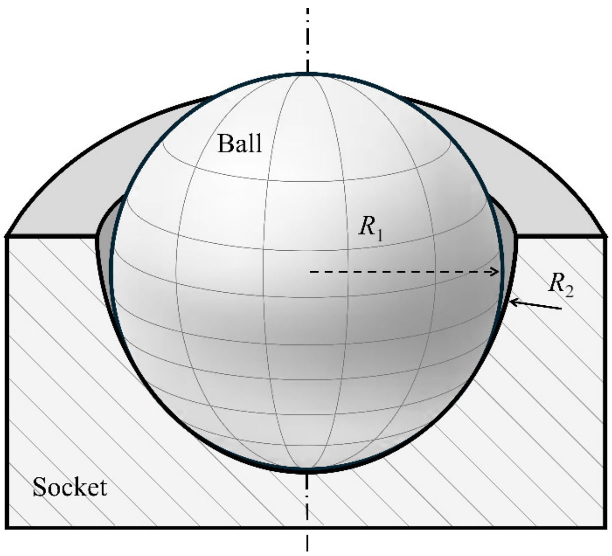


**Fig. 1** Conformal spherical contact between two elastic bodies (Ball and Socket). The sphere (Ball) has radius $R_1$. The spherical cavity (Socket) has radius $R_2$. The radial clearance is $C = R_2 - R_1 << R_1$.

[16–19]. Recently, in 2022 Jia and Chen [19] further explored the model proposed by Liu et al. [16] in 2006 by varying the materials and geometries and comparing the results with FEM. They proposed an empirical formula for the foundation modulus. However, the load–displacement curves still show some differences with respect to the FEM results. This is perhaps due to the intrinsic approximation of using an elastic foundation.

A different approach was taken by Tudor et al. in 2013 who provided a semianalytical method for a conformal spherical hard on soft contact based on Hills theory, under the hypothesis of the socket being an infinite elastic space [20]. Their method is iterative as it requires a guess of the contact area, followed by the resolution of a linear system of equations. They investigated contact pressure, contact radius and torque, finding a good agreement of the contact pressure with FEM results.

Given the assumptions required by the analytical formulas, the problem was also approached with computational methods. Most of the computational methods can be divided into the boundary element method (BEM) or FEM. In BEM, only the contact surface is meshed. Therefore, the hypothesis of half-space is not dropped. FEM is the most general method which nevertheless requires a greater computational cost. Kalker's exact theory of contact, which is BEM based, has been widely applied to wheel–rail rolling non-conformal contact [21]. Blanco-Lorenzo et al. [22] applied Kalker's theory to conformal wheel–rail contacts by introducing analytical approximate influence coefficients. Liu et al. [23] reviewed the methods for conformal wheel–rail contact.

Owing to the appeal of a more general method, many researchers used FEM to model spherical conformal contact. Comparisons between FEM and Hertz's theory for spherical conformal contacts were made by Lee and Polycarpou [24] in 2010 and by Sun and Hao [25] in 2012. Sun and Hao [25] pointed out that the FEM results gave a stiffer contact, a larger contact area, and a smaller contact pressure, compared to Hertz's theory. Lee and Polycarpou [24] observed opposite trends instead, if the spherical cavity was incomplete and the contact area saturated.

A combination of analytical and Finite Element methods was used by Fang et al. [26], who proposed in 2015 a universal approximate model for frictionless conformal complete spherical contacts, and later expanded it for incomplete spherical contacts [27]. Fang's model uses both analytical relations and empirical relations tuned by FEM. The solution is obtained iteratively as the model, though analytical, is not in closed form. The influence of socket thickness is considered negligible, as in Fang's model the socket thickness is not a variable. This is in contrast with analytical approximate results obtained with Winkler's foundation models, where the foundation modulus is a function of socket thickness [6, 14, 15, 17–19, 28]. Fang's model has been used to analyse roller cone drill bits journal bearings by He et al. [8] in 2016. In 2021, Yuan et al. [29] further investigated the role of friction and the free-edge effect in spherical plain bearings.

Experiments are fewer in number given the complexity of measuring pressure, stress, and contact area and given the increasing reliance on FEM for validation purposes. In 2016, Wu et al. [30] performed nanoindentation tests and FEM analyses of a spherical rigid indentation on a soft linearly elastic silicone support. They found out that Hertz's theory overestimates the contact pressure and underestimates the contact area. However, through a compensation of effects, the Hertz's load–displacement relation still approximately holds, if the silicone thickness is at least 20 times the indenter radius. In 2023, Mitchell et al. [31] pressed a rigid sphere against cubic gelatine and investigated the stresses experimentally through photoelasticity, comparing them with FEM. In 2010, Germaneau et al. [7] performed FEM analyses and experiments on a spherical aeronautical plain bearing. They analysed the displacement field through digital volume correlation and optical scanning tomography and investigated the impact of boundary conditions in the simulations. They concluded that the model with a deformable bearing fitting was closer to the experimental results with respect to the rigid fitting. In 2009, Childs and Harris [32] measured the stiffness of a TPJB Ball and

Socket pivot, which is an example of spherical conformal contact. However, they measured the stiffness of the entire pad support structure, composed by the pad, the Babbit layer, the contact between the rotor and the pad, the support shims, and the Ball and Socket pivot. They measured a constant stiffness, differently than the non-linear Hertzian relationship they were expecting [33]. In 2022, Ciulli et al. [9] measured the stiffness of a TPJB Ball and Socket pivot. The experimental load–displacement curve exhibited a higher stiffness compared to Hertz's theory.

As seen above, many approximate analytical and numerical methods have been developed for conformal spherical contacts and were compared with FEM analyses and experiments. Often the literature models involve some questionable assumptions, such as for instance neglecting the influence of the geometries or neglecting the effect of switching the materials of the ball and the socket, when those are composed by different materials. As reported in this paper, these assumptions can be inaccurate. To the best of the authors' knowledge, an empirical model based on the results of FEM simulations, without any a priori assumptions, apart from those used within the simulations, has not yet been presented. This paper aims at finding an analytical stiffness formula for the specific case of Ball and Socket contact with the simplifying assumption of axial symmetry. The methods followed for the FEM simulations are described in Section 2. The development of the empirical formula is described in detail in Section 3. The performance of the formula is evaluated in Section 4. Lastly, Sections 5 and 6 report the discussion, conclusions and future developments.

## 2 Materials and methods

2D axisymmetric FEM simulations were performed with the software ANSYS 2023 R1. Figure 2 defines the geometric parameters. Both bodies are axisymmetric and only their half-section is reported in Fig. 2.

The upper body, or ball, is a sphere of radius $R_1$, sectioned at a height $H$. The lower body, or socket, is derived from a cylinder of radius $R_1 + B$, height $H + B$, with a spherical cavity of radius $R_2$. A single parameter $B$ is used to jointly change the socket size, reducing the number of variables. Initially, the two unloaded bodies share a single point of contact, located on the axis of symmetry. The radial clearance $C$ is defined as $R_2 - R_1$.

The materials are linear elastic and therefore entirely characterized by their Young's modulus ($E$) and Poisson's modulus ($\nu$). They are $E_1$, $\nu_1$ for the ball and $E_2$, $\nu_2$, for the socket.

A uniform downward displacement $\delta$ is applied in increasing steps to the top, horizontal surface of the ball section (Fig. 2). The $\delta$ range used in the simulations approximately covers the elastic regime of the contact. No condition is imposed on the displacement along the plane orthogonal to the axis of symmetry (tangential displacement). The choice of imposing a uniform displacement instead of a uniform pressure is arbitrary. Actually, this choice has a significant effect, as reported previously by the authors in Ref. [34]. With a uniform pressure, the top surface bends, causing an increase of the contact area compared to the previous case, and making the contact stiffer. Therefore, due to the non-negligible difference between the two cases, the results contained in this paper should only be applied to systems where the upper displacement is uniform. This is the case of many practical applications such as TPJB ball and socket pivot.

The bottom horizontal surface of the socket is a frictionless rigid support, meaning that its vertical displacement is zero, while the tangential displacement is free. The contact between the ball and socket is frictionless. Actually, friction has an effect on the contact behaviour. In Ref. [34], the friction coefficient was varied from 0 up to 0.8, which is a relatively high value even for dry steel on steel contact. The difference in displacements due to friction reached up to 12%, with other quantities being equal. The socket support had marginal influence, with difference in displacements due to fixed or frictionless support not exceeding 3%. In practical applications, the contact pair is usually lubricated. Moreover, even for very high friction coefficient values, friction is not the dominant factor with respect to other boundary conditions. Therefore, in this paper the contact is kept frictionless.

The contact problem is therefore entirely specified by 8 parameters: $R_1$, $R_2$, $B$, $H$, $E_1$, $\nu_1$, $E_2$, and $\nu_2$. Note that for $H/R_1 = 1$, the upper body is a hemisphere.

Table 1 contains the elastic properties of the materials used in the simulations.

Table 2 contains the program simulation options. Options not reported in Table 2 are left program controlled, which means that the default values are used.

In the performed simulations the mesh contains from $10^4$ to $10^5$ nodes depending on the values of $B/R_1$, $H/R_1$. The edge sizing

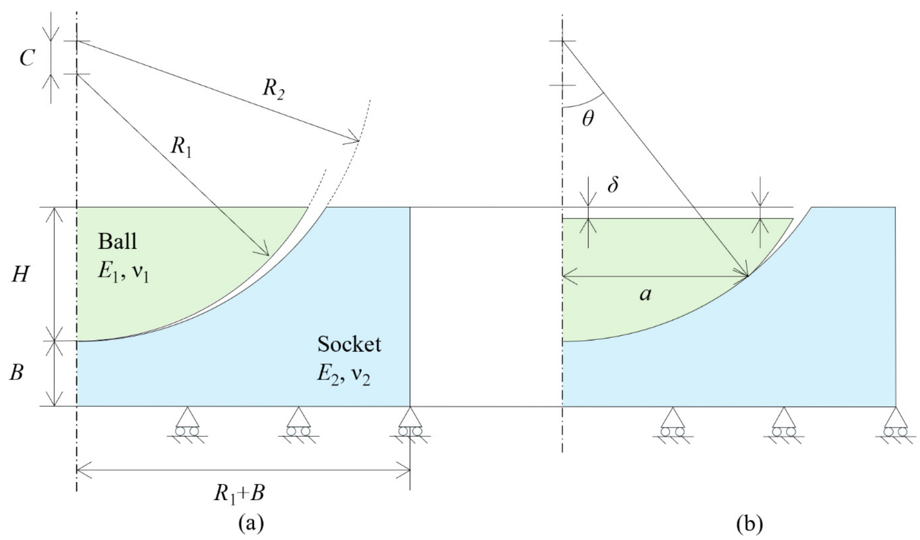


**Fig. 2** Geometry schematics used in the simulations. The bodies are axisymmetric, with only their half-section represented. The socket is placed on a rigid frictionless support (a) before loading and (b) after loading. Radius $a$ of contact area and contact angle $\theta$ are noted.

function is used to densify the mesh near the contact zone. The sensitivity of the results to the employed mesh was checked and it was found negligible for the used meshes (halving the number of nodes produced a relative difference of ~0.02% on $F$). An example of mesh and displacement map is reported in Fig. 3.

This work is particularly focused on the reaction force $F$ that the frictionless support exerts on the socket. Therefore, for each simulation, a load–displacement curve $F(\delta)$ is obtained and comparisons with the Hertzian results are also made. The system stiffness is then evaluated numerically by the derivative $\mathrm{d}F/\mathrm{d}\delta$.

## 3 Theoretical model

In classical Hertz's theory, the load–displacement relation for point contacts is

$$F(\delta) = \frac{2}{3}E'\sqrt{R'\delta^3} \tag{1}$$

where $E'$ is the equivalent elastic modulus and $R'$ is the equivalent radius, defined as

$$E' = 2\left(\frac{1-\nu_1^2}{E_1} + \frac{1-\nu_2^2}{E_2}\right)^{-1} \tag{2}$$

$$R' = \frac{R_2 R_1}{R_2 - R_1} = \frac{(R_1 + C)\,R_1}{C} \tag{3}$$

The contact stiffness is the derivative of the load–displacement relationship:

$$\frac{\mathrm{d}F(\delta)}{\mathrm{d}\delta} = E'\sqrt{R'\delta} \tag{4}$$

In Hertz's theory, the radius ($a$) of the projection of the contact area on the plane orthogonal to the axis of symmetry is equal to

$$a(\delta) = \sqrt{\delta R'} \tag{5}$$

Note that the value of the contact area ($\mathcal{A}$) is a simulation output while the value of the radius ($a$) of the projection of the contact area is not; therefore, $a$ has been calculated on a first approximation from $\mathcal{A}$ using the relations:

$$\mathcal{A} = 2\pi R_2^2(1-\cos\theta) \tag{6}$$

$$a = R_2 \sin\theta \tag{7}$$

where a contact angle ($\theta$) has been defined as the angle between the axis of symmetry and the line connecting the centre of the spherical surface of the socket, considered undeformed, to a point on the boundary of the contact (Fig. 2(b)).

Figure 4 compares FEM simulation results and Hertz's theory for a sample case. Figures 4(a) and 4(b) plot respectively the force ($F$) and contact radius ($a$) as a function of the body approach, here also called "displacement" ($\delta$).

As shown in Fig. 4(a), FEM simulation results give a stiffer contact compared to Hertz's theory. This is consistent with Refs. [9, 12, 16, 25]. In fact, Hertz's theory is valid for $\delta << a << R_1$. Since the values of $\delta$ are still very small, it must be concluded that the second inequality $a << R_1$ is not satisfied. This is verified in Fig. 4(b), which reports the FEM contact radius. In fact, at $\delta$ = 0.012 mm, $a$ is 10% of $R_1$, which may be taken as the arbitrary threshold beyond which the condition $a << R_1$ is invalid. At this

**Table 1** Elastic properties of materials used in simulations

| Material | $E$ (GPa) | $\nu$ |
|---|---|---|
| Structural steel (St) | 200 | 0.30 |
| Aluminum alloy (Al) | 71 | 0.33 |
| Titanium alloy (Ti) | 96 | 0.36 |

**Table 2** Program simulation options

| Contact | |
|---|---|
| Contact body | Ball |
| Target body | Socket |
| Contact formulation | Normal Lagrange |
| Small sliding | Off |
| Interface treatment | Adjust to touch |
| **Meshing** | |
| Meshing method | Quadrilateral dominant |
| General sizing element size | $R_1/10$ |
| Edge sizing element size, applied to contact surfaces | $R_1/50$ |
| Growth rate | 1.05 |
| Mesh refinement | 2 |
| **Analysis** | |
| Number of displacement steps | 1,000 |
| Maximum displacement $\delta_{max}$ | ~$8\times10^{-4}R_2$ |
| Displacement step size | $\delta_{max}/1,000$ |
| Weak springs | Off |
| Large deflections | On |
| Force convergence tolerance | $5\times10^{-5}$ |

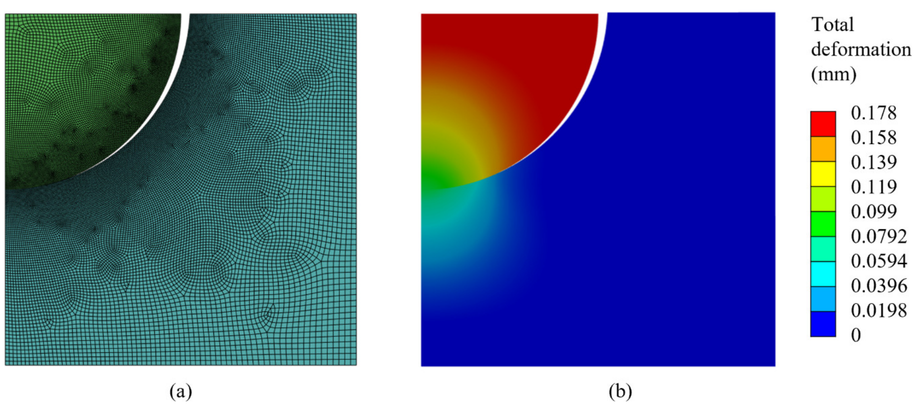


**Fig. 3** (a) Mesh and (b) displacement maps for $H = B = R_1$ = 23.72 mm, $R_2$ = 25 mm, and $\delta$ = 0.178 mm. The number of nodes is 72,641. The material is structural steel for both bodies.

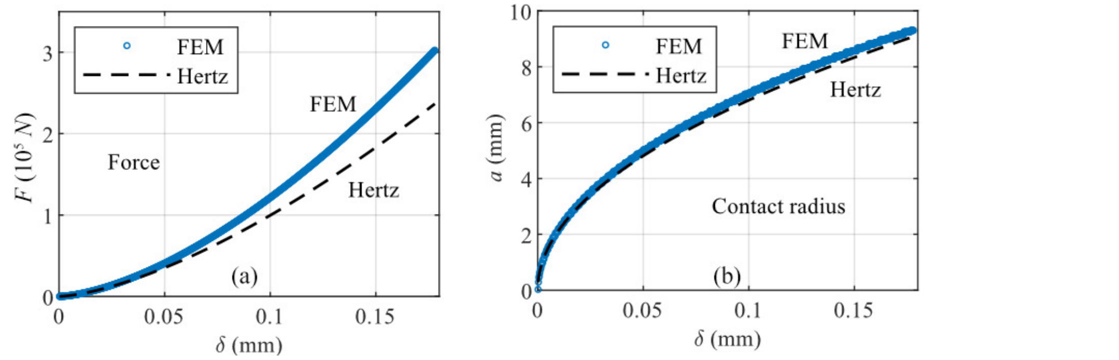


**Fig. 4** (a) Force $F$ vs. displacement $\delta$, (b) contact radius $a$ vs. displacement $\delta$. Comparison between FEM and Hertz's theory. $R_1 = B = H = 23.72$ mm, $R_2 = 25$ mm. The material is structural steel for both bodies.

threshold, the difference in load between Hertz and FEM is 7%, while at $\delta = 0.12$ mm it is 19%. As shown in Fig. 4(b), the FEM contact radius is slightly larger than that predicted by Hertz's theory. This is consistent with previous observations in Refs. [12, 25, 30]. Only the steel-on-steel contact is shown here but the simulation of other materials (Table 1) gives similar results.

In Sections 3.1 and 3.2, further simulations are performed, leading to some useful relations.

### 3.1 Scale invariance

In Hertz's theory it is customary to define non-dimensional quantities for force ($\mathcal{L}$) and displacement ($d$):

$$\mathcal{L} = \frac{3F}{2E'R'^2} \tag{8}$$

$$d = \frac{\delta}{R'} \tag{9}$$

Figure 5(a) shows several FEM results ($F$ vs. $\delta$) obtained with constant ratio $R_1/R_2 = 0.9488$ and compares them with Hertz's theory. Figure 5(b) reproduces the same data in non-dimensional units ($\mathcal{L}$ vs. $d$). Note that while the cases reported in Fig. 5 have different clearances $C$, they have the same relative clearance ($C/R_2 = 1 - R_1/R_2$).

As shown in Fig. 5(b) Hertz's theory reduces to a single curve. This is not particularly surprising as the non-dimensional expression for Eq. (1) is $\mathcal{L} = d^{3/2}$. While the definition of quantities such as $\mathcal{L}$ and $d$ depends on $R'$, the function $\mathcal{L} = d^{3/2}$ itself does not depend on any parameters, when plotted in non-dimensional units (Fig. 5(b)). Moreover, as shown in Fig. 5(b) the FEM results with the same relative clearance also overlap on a single (and different) curve. This observation was verified also in other simulations with different ratios $R_1/R_2$, different $B/R_1$ and $H/R_1$ ratios, and different materials (Table 1). In practice, this means that if all the geometrical quantities of the problem ($B$, $H$, $R_1$, and $R_2$) are multiplied by the same arbitrary factor, the $\mathcal{L}(d)$ curve obtained from FEM does not change. Or, in short, it is verified that $\mathcal{L}(d)$ is invariant to scale. This is indeed a useful observation because it allows to simulate results at an arbitrary scale, and that is an arbitrary choice of the value of $R_2$, without loss of generality. In this paper, the value of $R_2$ was set to 25 mm for most simulations.

### 3.2 Stiffness asymptote

In this section we investigate the effect of clearance $C = R_2 - R_1$ on the simulation results. Figure 6(a) reports several load–displacement curves obtained by FEM. Figure 6(b) plots instead their numerical derivative. Note that the stiffness data were smoothed with a moving average filter. The smoothing operation has a negligible effect on the curves, although it filters out some numerical noise, making data visualization easier. The simulations were performed at different clearances $C$ according to a geometric series: $C_0$, $2C_0$, …, $2^9C_0$, with $C_0 = 2.5$ μm and $R_2 = 25$ mm. The geometric series allows to probe a wide range of clearances with a limited number of test cases.

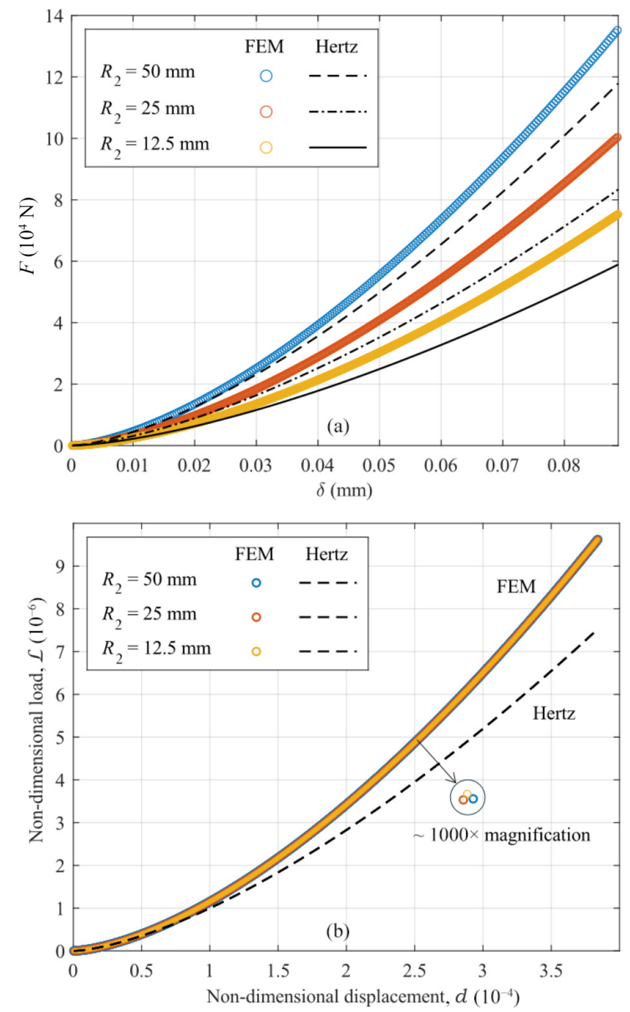


**Fig. 5** (a) Force $F$ vs. displacement $\delta$; (b) non-dimensional force $\mathcal{L}$ vs. non-dimensional displacement $d$. Comparison between FEM and Hertz's theory. $B = H = R_1 = 0.9488R_2$. The material is structural steel for both bodies.

It is interesting to note from Fig. 6(b) that the low clearance curves ($C$ = 0.0025 mm to $C$ = 0.04 mm) share a stiffness asymptote ($k_\infty$) which does not depend on $C$. The high clearance

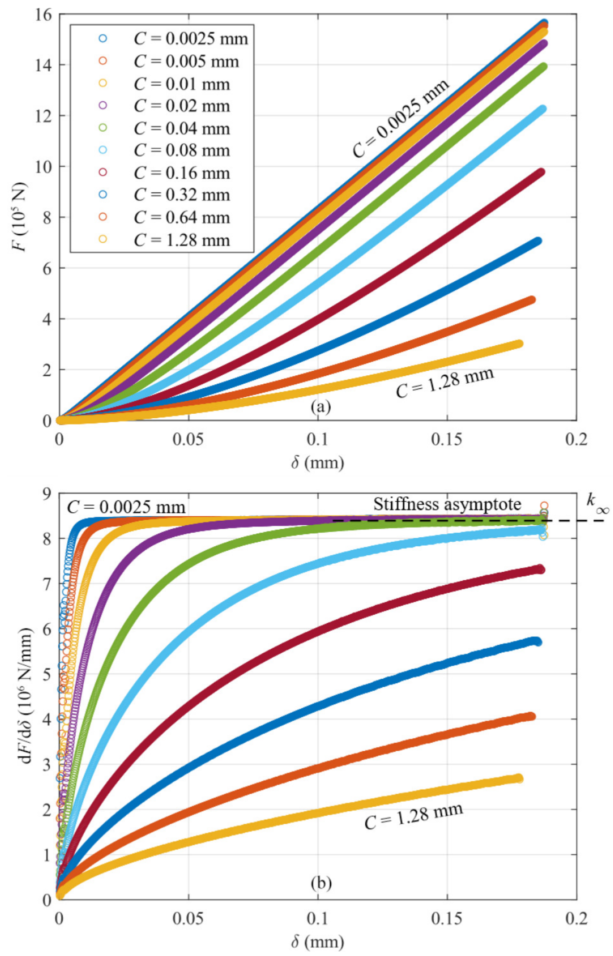


**Fig. 6** (a) Force $F$ vs. displacement $\delta$; (b) stiffness $\mathrm{d}F/\mathrm{d}\delta$ vs. displacement $\delta$. FEM results with $B = H = R_1$, $R_2 = 25$ mm. The material is structural steel for both bodies.

curves ($C$ = 0.08 mm to $C$ = 1.28 mm) instead do not explicitly show this property in Fig. 6(b) because they are truncated at $\delta \approx 0.18$ mm. However, they would also reach the stiffness asymptote ($k_\infty$), if Fig. 6(b) included higher $\delta$ values, as it was separately verified (not shown in Fig. 6(b)). The existence of this stiffness asymptote independent on clearance was also further verified in many simulations for different materials (Table 1), and ratios $B/R_1$ and $H/R_1$. It was observed that the value of $k_\infty$ changes with materials, $B/R_1$, and $H/R_1$. The existence of this asymptote marks a striking difference from Hertz's theory, where the stiffness is unbounded. As it is verified in Fig. 7, the stiffness asymptote occurs when the contact area saturates, which provides an intuitive physical justification. Alternatively, $k_\infty$ can be defined as the system stiffness with $C = 0$.

In short, the stiffness asymptote property is written as

$$\lim_{\delta\to\infty}\frac{\partial F(\delta)}{\partial \delta} = k_\infty \tag{10}$$

which corresponds to a force asymptote:

$$\lim_{\delta\to\infty} F(\delta) = q_\infty + k_\infty \delta \tag{11}$$

where $q_\infty$ and $k_\infty$ are unknown parameters. Estimation of $q_\infty$ can be bypassed by dealing with the stiffness instead of the force. In practical applications, such as for spherical pivots in TPJB, usually the stiffness is required. Moreover, the load–displacement relation can be derived by numerical integration. For these reasons, the

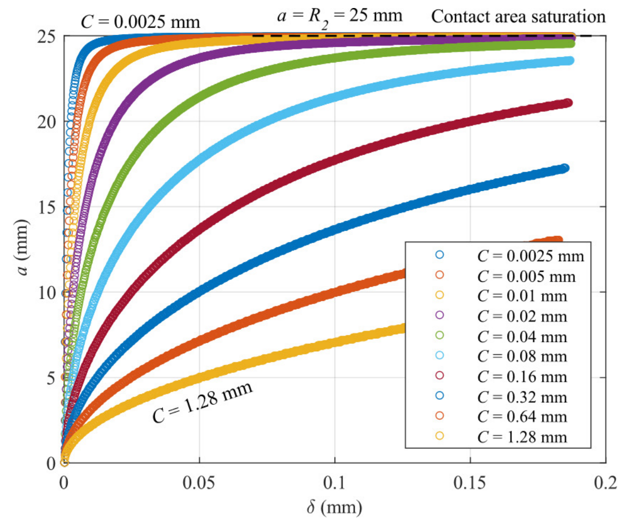


**Fig. 7** Contact radius $a$ vs. displacement $\delta$. FEM results with $B = H = R_1$, $R_2$ = 25 mm. The material is structural steel for both bodies.

authors, in Sections 3.3 and 3.4, focus on the stiffness–displacement relation.

Equation (10) can be rewritten in non-dimensional units:

$$\lim_{d\to\infty}\frac{\partial \mathcal{L}(d)}{\partial d} = \frac{3}{2}\frac{k_\infty}{E'R_2}\left(\frac{R_2}{R_1}-1\right) \tag{12}$$

Since $\mathcal{L}(d)$, $R_2/R_1$, and $E'$ are scale invariant, it is concluded from Eq. (12) that also $k_\infty/R_2$ must be scale invariant, which means that $k_\infty$ linearly scales with size. Recall that $\mathcal{L}(d)$ was shown to be scale invariant in Section 3.1, while $R_2/R_1$ and $E'$ are scale invariant by definition: if all geometrical quantities are multiplied by the same arbitrary factor, a scale invariant quantity does not change. In particular, $R_2/R_1$ is scale invariant because it is a ratio of two geometrical quantities. $E'$ is scale invariant because it does not depend on geometry. The fact that $k_\infty/R_2$ is scale invariant was also directly verified in a series of simulations. In summary, $k_\infty/R_2$ is an unknown function of $B/R_1$, $H/R_1$, and the material properties.

### 3.3 Clearance invariance

In this section we show that through an ad hoc normalization of displacement and stiffness, FEM stiffness curves obtained with different clearances can be reduced to a single one ranging from 0 to 1. This normalization was found based on previous observations reported in Sections 3.1 and 3.2. The normalized displacement $\delta'$ and stiffness $(\mathrm{d}F/\mathrm{d}\delta)'$ are defined as

$$\delta' = \frac{E'^2 R' \delta}{k_\infty^2} \tag{13}$$

$$\left(\frac{\mathrm{d}F}{\mathrm{d}\delta}\right)' = \frac{1}{k_\infty}\frac{\mathrm{d}F}{\mathrm{d}\delta} \tag{14}$$

When dealing with conformal contact, this novel normalization is to be preferred to the conventional one (Eqs. (8) and (9)) because with the proposed one the stiffness curves with different clearances reduce to a single one while with the conventional one they do not. Note that Eqs. (13) and (14) utilize the stiffness asymptote ($k_\infty$) defined previously in Section 3.2. This normalization is non-dimensional. It maps Hertz's theory into a square root $\left((\mathrm{d}F)/(\mathrm{d}\delta)\right)' = \sqrt{\delta'}$ and maps the stiffness asymptote into the horizontal line $\left((\mathrm{d}F)/(\mathrm{d}\delta)\right)' = 1$. To show the effect of the renormalization on simulation data, in Fig. 8, the curves previously shown in Fig. 6(b) are renormalized according to Eqs. (13) and (14).

Figure 8 shows that although the simulations are performed at different clearances, through the renormalization defined in Eqs. (13) and (14) the results overlap on a single "master" curve. This is indeed very useful information because it allows to consider a fitting model independent on clearance. Note that in Fig. 8 curves with higher clearance (lower $R'$) span a smaller range of the $\delta'$ axis. The curves with lower clearance (higher $R'$) are overlapped by the others and span a higher $\delta'$ range, exceeding the bounds of Fig. 8. These also have higher $\delta'$ step size and show some outliers which are likely due to numerical errors in the simulation. The presence of a clearance-independent curve was also verified for different cases, such as different combination of materials (Table 1) and variation of the ratios $B/R_1$ and $H/R_1$. Each "master" curve is different to some extent depending on the materials, $B/R_1$ and $H/R_1$ (see Appendix A). In summary, in conformal spherical contacts, the stiffness renormalized according to Eqs. (13) and (14) is invariant with clearance ($C$). However, the shape of the clearance-invariant curve changes with $B/R_1$, $H/R_1$, and the materials parameters. A prerequisite of an accurate stiffness model is to be able to represent and adapt well to these curves. This issue will be solved in Section 3.4.

### 3.4 Analytical stiffness function

An accurate stiffness model for conformal spherical contacts aims to interpolate the family of functions ($\mathrm{d}F/\mathrm{d}\delta'$ vs. $\delta'$) which can be obtained by varying $B/R_1$, $H/R_1$, $E_1$, $E_2$, $\nu_1$, and $\nu_2$. The search space is restricted by the following considerations:

(1) The new model must agree with Hertz's theory for small values of $\delta'$, that is, large clearances or small displacements. This mathematically translates to

$$\lim_{\delta' \to 0} \left(\frac{\partial F}{\partial \delta}\right)' = \sqrt{\delta'} \tag{15}$$

(2) The new model must be consistent with the stiffness asymptote empirically observed in Section 3.2. This mathematically translates to

$$\lim_{\delta' \to \infty} \left(\frac{\partial F}{\partial \delta}\right)' = 1 \tag{16}$$

(3) Although countless functions can indeed be found to fit the problem, simplicity is to be preferred along with a reasonable accuracy. While this is a qualitative requirement, each model accuracy is quantified with the procedure reported in Section 4.1. "Simplicity" in a broad sense means a shorter equation and fewer free parameters.

The search of the fitting function has been the most difficult and time-consuming part of this work. The authors tested several functions, not reported here for brevity (Appendix B), evaluating their accuracy with the procedure reported in Section 4.1 and also rating their simplicity. It is the opinion of the authors that a function with two free parameters gives the best compromise between accuracy and simplicity. Finally, amongst the tested functions with two free parameters, the function with the least error was

$$\left(\frac{\partial F}{\partial \delta}\right)' = \left(1 - \exp\left(-\sqrt{\delta'}^{\,m} - \left(\lambda\delta'\right)^{m}\right)\right)^{\frac{1}{m}} \tag{17}$$

where $\lambda$ and $m$ are free parameters. Together with $k_\infty$, which is needed for the definition of $\delta'$ (Eq. (13)), there are three unknown parameters ($k_\infty$, $\lambda$, $m$). The parameters depend in a complex way on $B/R_1$, $H/R_1$, $E_1$, $E_2$, $\nu_1$, and $\nu_2$. In order to complete the model, $k_\infty$, $\lambda$, and $m$ must be fitted to the results of simulations, as will be carried out in Section 4. Note that Eq. (17) satisfies both necessary conditions Eqs. (15) and (16). The condition in Eq. (15) can be verified by calculating the Taylor series of Eq. (17) in $\delta = 0$.

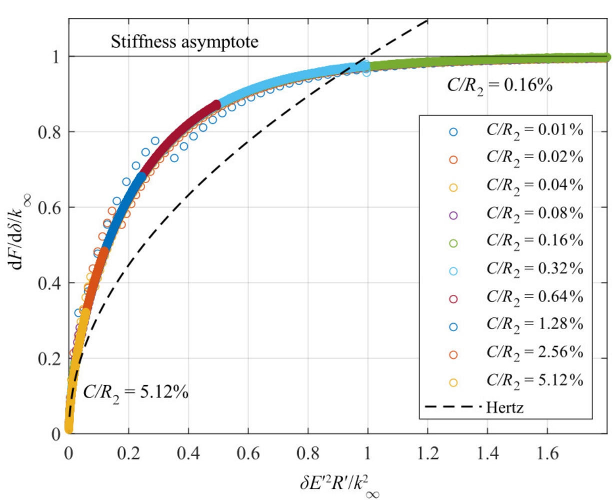


**Fig. 8** Normalized stiffness vs. normalized displacement. FEM results with $B = H = R_1$, $R_2 = 25$ mm. The material is structural steel for both bodies. The stiffness asymptote is fitted to the simulation data with $k_\infty \approx 8.4\times10^6$ N/mm.

## 4 Results

### 4.1 Tabulated parameters and model comparison

Here, the free parameters ($k_\infty$, $\lambda$, $m$) are found by best fitting Eq. (17) to FEM results. The error to be minimized is the root mean square of the difference between the dimensional model stiffness and the dimensional FEM stiffness. The optimization was carried out with multiple starting points, in order to be reasonably sure that the global minimum is found. The error map was investigated thoroughly, and no local minima were found other than the global minimum.

In Table 3 the results of the optimization procedure are reported. For each row in Table 3 multiple FEM simulations were carried out, similarly to Fig. 6, with clearance ranging from $C_0$, $2C_0$, …, $2^9C_0$, with $C_0$ = 2.5 μm and $R_2$ = 25 mm. However, differently from Fig. 6, the materials properties and $B/R_1$ and $H/R_1$ ratios were varied according to each row of Table 3. Plots similar to Fig. 8 for each row of Table 3 are reported in Appendix A.

In the last column of Table 3, the ratio between the stiffness error and $k_\infty$ (a reference value) is reported. This value did not exceed 0.8% in any row of Table 3, confirming the accuracy of the model in fitting the data. The entries for Table 3 were chosen to provide sufficient variety. All possible combinations of Table 1 materials are reported with $B = H = R_1$ from row 1 to row 8. From row 9 to row 11, the geometry of the ball is changed and from row 12 to 14, the geometry of the socket is changed. It can be noted that $k_\infty/R_2$ depends both on the materials and the geometry. Its value increases for stiffer materials. The $\lambda$ and $m$ values are most sensitive to the geometry.

To critically assess the new model performance, Figs. 9 and 10 also compare other popular theories for spherical conformal contacts. While many models exist, as reported in the Introduction, we chose to compare the most influential (most cited) ones at the time of writing, amongst recent models, not older than 20 years. These are the models from Liu et al. [16] and Fang et al. [26]. Liu's model is based on a Winkler's foundation

**Table 3** Optimal parameters for given geometries and material properties

| # | Mat 1* | Mat 2* | $H/R_1$ | $B/R_1$ | $k_\infty/R_2$ (GPa)† | $\lambda$ | $m$ | Error/$k_\infty$ |
|---|---|---|---|---|---|---|---|---|
| 1 | St | St | 1 | 1 | 336 | 2.64 | 1.02 | 0.0021 |
| 2 | Al | Al | 1 | 1 | 123 | 2.62 | 1.03 | 0.0020 |
| 3 | Ti | Ti | 1 | 1 | 171 | 2.58 | 1.04 | 0.0020 |
| 4 | St | Al | 1 | 1 | 159 | 2.79 | 0.90 | 0.0045 |
| 5 | Al | St | 1 | 1 | 215 | 2.85 | 1.34 | 0.0037 |
| 6 | Ti | St | 1 | 1 | 272 | 3.00 | 1.29 | 0.0037 |
| 7 | Ti | Al | 1 | 1 | 140 | 2.73 | 0.98 | 0.0024 |
| 8 | St | Ti | 1 | 1 | 198 | 2.54 | 0.92 | 0.0038 |
| 9 | St | St | 0.5 | 1 | 404 | 6.96 | 1.57 | 0.0026 |
| 10 | St | St | 0.25 | 1 | 351 | 10.6 | 1.74 | 0.0040 |
| 11 | St | St | 0.125 | 1 | 260 | 11.5 | 1.74 | 0.0076 |
| 12 | St | St | 1 | 0.5 | 338 | 3.51 | 0.95 | 0.0021 |
| 13 | St | St | 1 | 0.25 | 332 | 4.59 | 0.85 | 0.0023 |
| 14 | St | St | 1 | 0.125 | 320 | 5.70 | 0.76 | 0.0030 |

*St = structural steel, Al = aluminum alloy, Ti = titanium alloy. Materials properties in Table 1. † Recall that $k_\infty/R_2$ is scale invariant.

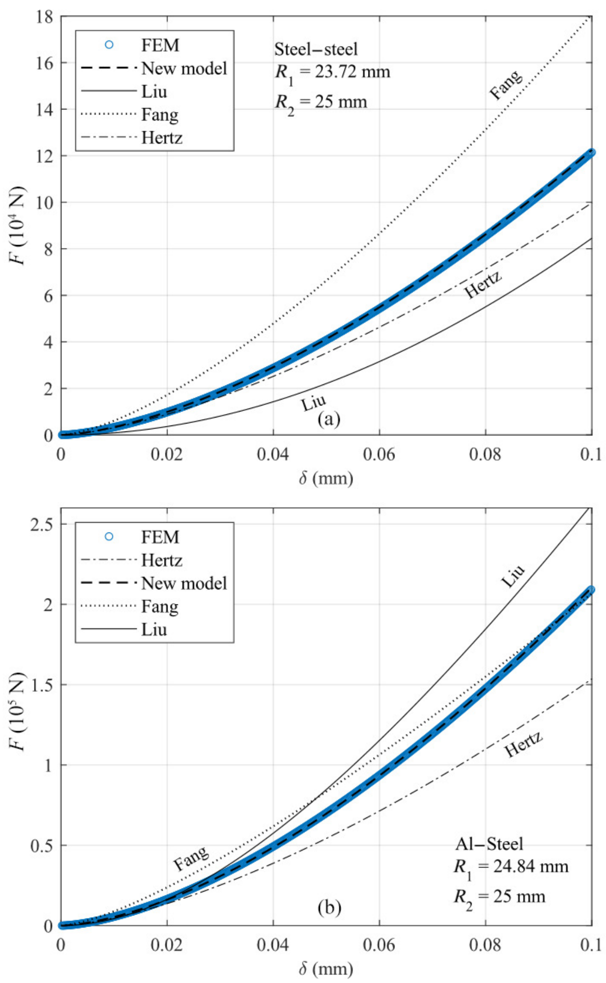


**Fig. 9** Force ($F$) vs. displacement ($\delta$). Comparison between FEM, new proposed model, Liu's, Fang's, and Hertz's theory (a) $R_1$ = 23.72 mm. $R_2$ = 25 mm. Material 1: steel. Material 2: steel. $B = H = R_1$. $k_{Liu}$ = 1.03 (b) $R_1$ = 24.84 mm. $R_2$ = 25 mm. Material 1: aluminum. Material 2: steel. $B = H = R_1$. $k_{Liu}$ = 1.24. $k_{Liu}$ obtained by fitting the FEM stiffness asymptote.

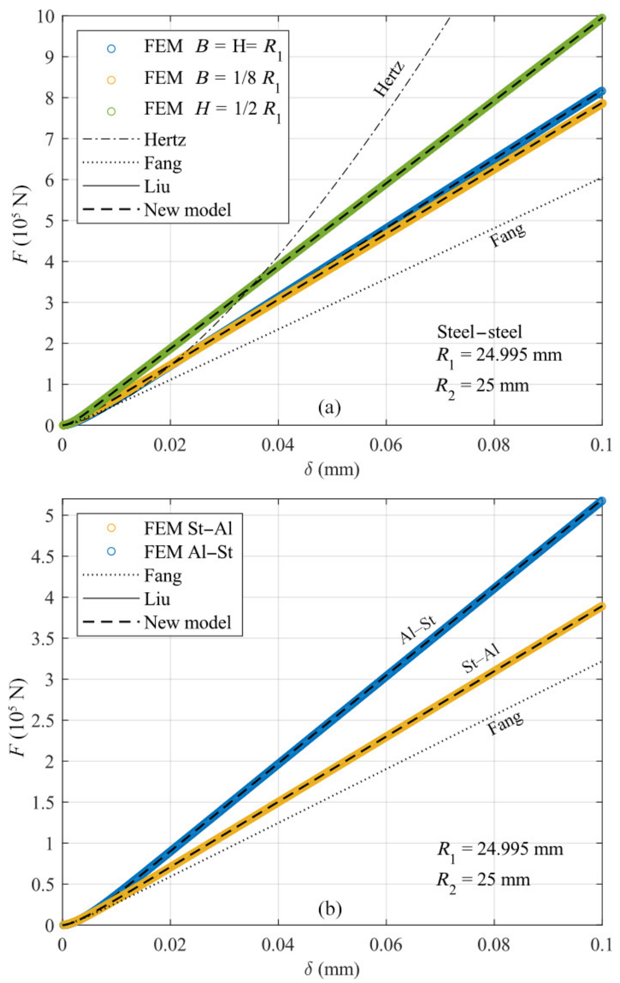


**Fig. 10** Force ($F$) vs. displacement ($\delta$). Comparison between FEM, new proposed model, Liu's, Fang's, and Hertz's theory. Liu's results, not visible, are covered by FEM data. (a) Comparison among different geometries. $R_1$ = 24.995 mm. $R_2$ = 25 mm. Material 1: steel. Material 2: steel. Several $B$ and $H$ values. First case: $B = H = R_1$. Second case: $B$ = 1/8 $R_1$, H = $R_1$. Third case: $B = R_1$, $H$ = ½$R_1$. (b) Comparison among different materials. $R_1$ = 24.995 mm. $R_2$ = 25 mm. Material 1: steel or aluminum. Material 2: aluminum or steel. $B = H = R_1$.

hypothesis. In Liu's model, the load–displacement relation is $F = k_{\mathrm{Liu}}(2\pi E' R_2 \delta^2)\sqrt{(2C+\delta)/[2(C+\delta)]}/[3(C+\delta)]$, with $k_{\mathrm{Liu}}$ being a model free parameter. Fang's model is based instead on a combination of empirical FEM results and analytical assumptions, leading to a system of equations to be solved iteratively. In Fang's model, the load–displacement relation is obtained numerically. The models and their derivation are fully described in their respective references [16, 26]. Significant care has been placed in the implementation of Liu's and Fang's models by first correctly replicating the results reported in their respective references. Figures 9 and 10 compare the force ($F$) vs. displacement ($\delta$) relationship for different models. The new model free parameters ($k_\infty$, $\lambda$, $m$) were taken from Table 3. In order to ease comparison among different formulations a direct dimensional approach was preferred, avoiding manipulation of the results of Liu's and Fang's models. Thus, Eq. (17) was dimensionalized through Eqs. (13) and (14). Then, the $F$ vs. $\delta$ curve was obtained through numerical integration of the (d$F$/d$\delta$) vs. $\delta$ curve. Figure 9 compares theories and FEM results for two different values of clearances. Figure 10 compares instead different geometries (Fig. 10(a)) and different materials (Fig. 10(b)).

Note that while Hertz's model has unbounded stiffness (Fig. 10(a)), both Liu's and Fang's models correctly have a stiffness asymptote. For Liu's model, the stiffness asymptote is proportional to $k_{\mathrm{Liu}}$: $\lim_{\delta\to\infty} F = \sqrt{2}\pi k_{\mathrm{Liu}} E' R_2 \delta/3$. Fang's stiffness asymptote instead is shown to be present by plotting it numerically (Fig. 10). In this respect, both Liu's and Fang's models are improvements of Hertz's formula. However, in the limit of small displacements, for Liu it is $F \sim \delta^2$, not coherent with Hertz's theory $F \sim \delta^{3/2}$. In Fig. 9, $k_{\mathrm{Liu}}$ was chosen to fit the FEM stiffness asymptote, thus in agreement with the simulation results at high displacements. Nevertheless, by doing so, Liu's model gives poor predictions at low displacements (Fig. 9).

Fang's model instead has no free parameters. It provides interesting results also for pressure and contact area. However, it uses excessively restrictive assumptions as it does not distinguish between different geometries, as it is done here by varying the $B/R_1$, $H/R_1$ ratios, giving for instance a unique curve in Fig. 10(a). Furthermore, Fang's model assumes "material symmetry", with no differences in predictions if the Ball and Socket materials are switched. The inadequacy of this hypothesis is shown in Fig. 10(b). The novel proposed model allows for more flexibility having three free parameters, giving higher accuracy in a variety of conditions, also with different $B/R_1$, $H/R_1$ ratios, and materials. The drawback of this is the larger number of free parameters ($k_\infty$, $\lambda$, $m$) whose estimation will be addressed in Section 4.2.

## 4.2 Parameters estimation

In order not to rely on the FEM results to find the free parameters ($k_\infty$, $\lambda$, $m$), their analytical dependence on $B/R_1$, $H/R_1$, $E_1$, $E_2$, $\nu_1$, $\nu_2$ needs to be found. Recall that $k_\infty$ is the system stiffness with zero clearance, while $\lambda$ and $m$ are empirical parameters. While this task deserves further deeper investigations that will be performed in a future work, sample formulas obtained for a subset of conditions are reported in this section.

Here, we considered the contact problem with $H = B = R_1$, $\nu_1 = \nu_2 = 0.3$, and variable $E_1$ and $E_2$. The elastic moduli were varied from 10 to 200 GPa. For each data point in Figs. 11 and 12, a FEM simulation with 1.6 ‰ clearance was performed ($R_1$ = 24.96 mm, $R_2$ = 25 mm), with 1,000 displacement steps from 0 up to $\delta_{\max}$ (Table 2). This choice of clearance and $\delta_{\max}$ covers adequately the "master curve" in Fig. 8, allowing to find the correct fit for parameters ($k_\infty$, $\lambda$, $m$). Despite simulating only a single clearance, the results are valid for any clearance as the "master curve" is clearance-invariant. These approximate empirical relations are found, valid for any $R_2$:

$$k_\infty = \frac{E_1 E_2 R_2}{0.3635 E_1 + 0.2303 E_2} \tag{18}$$

$$\lambda = \begin{cases} 2.523 + 1.247\exp\left(-2.484\dfrac{E_2}{E_1}\right), & \dfrac{E_2}{E_1} \le 2.05 \\ 3.029 - 0.6305\exp\left(-0.1141\dfrac{E_2}{E_1}\right), & \dfrac{E_2}{E_1} > 2.05 \end{cases} \tag{19}$$

$$m = 1.800 - 1.017\exp\left(-0.2675\frac{E_2}{E_1}\right) \tag{20}$$

The fit of Eqs. (18)–(20) to the data is shown in Figs. 11 and 12.

The approximate empirical relations (Eqs. (18)–(20)) are deemed satisfactory, as the difference with FEM values does not exceed 4% for $k_\infty$, 0.4% for $\lambda$, and 2% for $m$. The authors have also preliminary investigated the influence of the Poisson's ratio in a

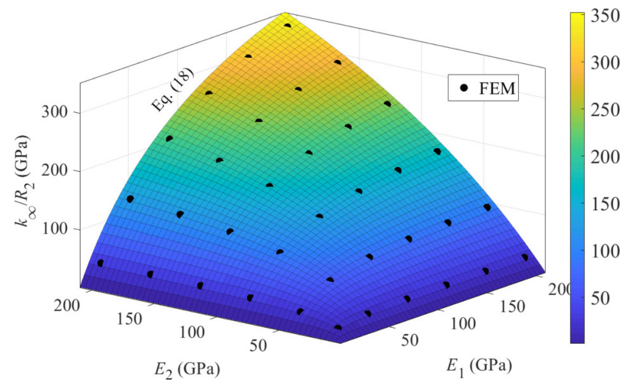


**Fig. 11** $k_\infty/R_2$ vs. $E_1$, $E_2$ for the contact problem with $B = H = R_1$, and $\nu_1 = \nu_2 = 0.3$.

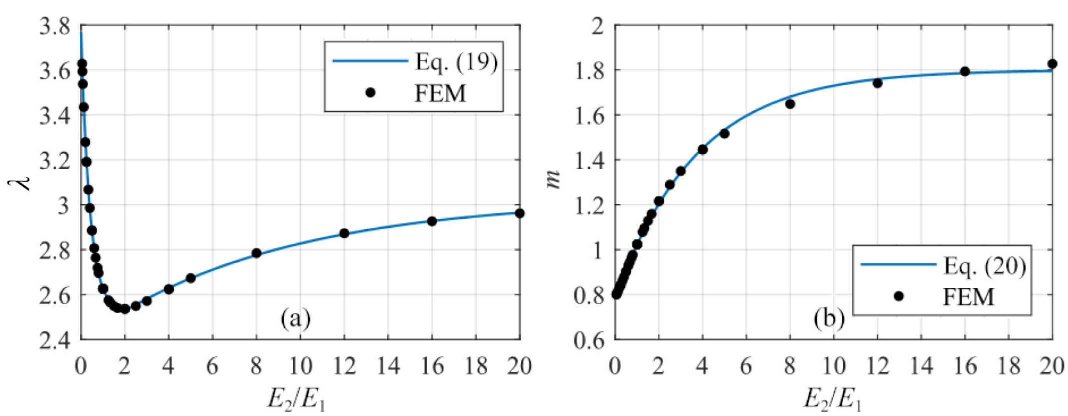


**Fig. 12** (a) $\lambda$ vs. $E_2/E_1$, (b) $m$ vs. $E_2/E_1$ for contact problem with $B = H = R_1$, and $\nu_1 = \nu_2 = 0.3$.

series of simulations not reported here. The results seem to show that it is not possible to use the conventional definition of elastic modulus (Eq. (2)) as a model invariant. However, this aspect deserves further study, and it is out of the scope of the present work.

## 5 Discussion

The novel stiffness model for spherical conformal contacts is here summarized. The contact problem is defined by its geometry (Fig. 2): $R_1$, $R_2$, $B$, and $H$ and its material properties: $E_1$, $E_2$, $\nu_1$, and $\nu_2$. A closed-form solution is available for a subset of the parameters space, that is $B = H = R_1$, $\nu_1 = \nu_2 = 0.3$, and $E_1, E_2 \in [10, 200]$ GPa. In this case, the free parameters ($k_\infty$, $\lambda$, $m$) are calculated analytically with Eqs. (18)–(20). For all the other cases, $k_\infty$, $\lambda$, and $m$ need to be tuned by FEM, as described in Section 4.2. The normalized displacement $\delta'$ is then calculated with Eq. (13). The normalized stiffness is calculated with Eq. (17). Finally, the stiffness is calculated with Eq. (14). The force may be calculated from the stiffness by numerical integration. The standard definitions of equivalent modulus ($E'$) and radius ($R'$), used in the formula above, are recalled in Eqs. (2) and (3).

The contact behaviour is partitioned in three regimes: the Hertzian regime, for $\delta' \to 0$, a transition regime, and a constant stiffness regime, for $\delta' \gtrsim 1$, depending on the actual values of the contact parameters. The constant stiffness regime corresponds to the saturation of the contact area.

The existence of a clearance-invariant curve allows to reduce computational time as the ($k_\infty$, $\lambda$, $m$) values can be obtained by simulating a single clearance value, as described in Section 4.2.

The major drawback of this model is that it requires estimation by FEM of three free parameters (apart from the analytical subset of solutions above). Future work will extend the closed-form solution to other cases of practical interest. Furthermore, the model limitations are

(1) It is valid only for linear elastic materials, not plastic.

(2) It is valid only for static load, not dynamic loads.

(3) It does not include the effect of transversal or non-centred loads.

Regarding limitation (1), although in conformal contacts the contact stress is lower than the predicted one from Hertz's theory [25, 30], a loading threshold exists where plastic deformation occurs. The stiffness with plasticity is expected to be lower than that predicted by the purely elastic model [35]. Addressing this limitation requires complicating the model further with the plastic properties of the materials. Regarding limitation (2), it could be addressed by considering a complex valued elastic modulus. Limitation (3) would require the introduction of friction but it can in principle be studied with a similar methodology.

## 6 Conclusions

A novel model for the stiffness of conformal elastic spherical contacts is introduced. The model fits accurately FEM results and reduces back to Hertz's theory in the limit of non-conformal contacts. The model requires three unknown free parameters ($k_\infty$, $\lambda$, $m$) which, in general, need to be tuned by FEM. Analytical approximate expressions for $k_\infty$, $\lambda$, and $m$ are provided for a simplified case with a given geometry and with Poisson's modulus equal to 0.3 for both bodies. By doing so, a non-dimensional stiffness–displacement curve is defined, which is invariant to the contact clearance, allowing to save computational time.

The results contained here can be useful to better represent the behaviour of conformal spherical contacts of practical interest with respect to the already existing analytical models. A general analytical expression for $k_\infty$, $\lambda$, and $m$ will be investigated in the future.

Future work will also consider the contact area and pressure distribution.

## Appendix A

A selection of clearance-invariant curves with different material parameters and $B/R_1$, $H/R_1$ ratios is shown in Fig. A1.

The clearance-invariance property holds in different cases although the curve shape changes with different materials or different ratios $B/R_1$ and $H/R_1$. The new model (Eq. (17)) adapts well to the FEM results.

## Appendix B

In this Appendix, the list of the main fitting functions tested is reported for completeness. Some stand-alone functions are tested; others can be obtained from function sets. Two sets of functions are reported (Eqs. (B1) and (B2)):

$$\frac{\partial F}{\partial \delta} = k_\infty \left(1 - \frac{1}{1 + \sqrt{\delta'} + g}\right) \tag{B1}$$

In Eq. (B1), any function $g\left(\delta'\right)$ can be substituted, provided that $g(0) = 0$, $g(\infty) = \infty$, and the Taylor series of $g$ in 0 has power terms equal or greater than 1.

$$\frac{\partial F}{\partial \delta} = k_\infty \left[(g_1 - g_2) g_3 + g_2\right] \tag{B2}$$

In Eq. (B2), any function $g_1\left(\delta'\right)$, $g_2\left(\delta'\right)$, and $g_3\left(\delta'\right)$ can be substituted, provided that $\lim\limits_{\delta' \to 0} g_1 \sim \sqrt{\delta'}$, $\lim\limits_{\delta' \to \infty} g_2 = 1$, $g_3(0) = 1$, $g_3(\infty) = 0$, and $g_3$ monotonically decreasing.

The main tested functions are grouped below according to their number of free parameters.

Functions with one parameter ($k_\infty$):

$$\frac{\partial F}{\partial \delta} = k_\infty \left(1 - \mathrm{e}^{-\delta'}\right)^{\frac{1}{2}} \tag{B3}$$

Note: Eq. (B3) is not accurate enough.

Functions with two parameters ($k_\infty, \lambda$):

$$\frac{\partial F}{\partial \delta} = k_\infty \left(1 - \mathrm{e}^{-\delta'^{\lambda}}\right)^{\frac{1}{2\lambda}} \tag{B4}$$

Note: Eq. (B4) can never be higher than Hertz's. Not accurate.

$$\frac{\partial F}{\partial \delta} = k_\infty \left(1 - \mathrm{e}^{-\left(\sqrt{\delta'} - \lambda \delta'\right)}\right) \tag{B5}$$

Note: Eq. (B5) is obtained from Eq. (B2) with $g_1 = 1 - \mathrm{e}^{-\sqrt{\delta'}}$, $g_2 = 1$, and $g_3 = \mathrm{e}^{-\lambda\delta'}$. It is promising, although not accurate enough and not flexible enough.

$$\frac{\partial F}{\partial \delta} = k_\infty \left(\tanh \delta'^{\lambda}\right)^{\frac{1}{2\lambda}} \tag{B6}$$

Note: Eq. (B6) can never be higher than Hertz's. Not accurate.

$$\frac{\partial F}{\partial \delta} = k_\infty \left(1 - \frac{1}{1 + \sqrt{\delta'} + \lambda \delta'}\right) \tag{B7}$$

Note: Eq. (B7) is obtained from Eq. (B2) with $g = \lambda \delta'$. Not accurate enough.

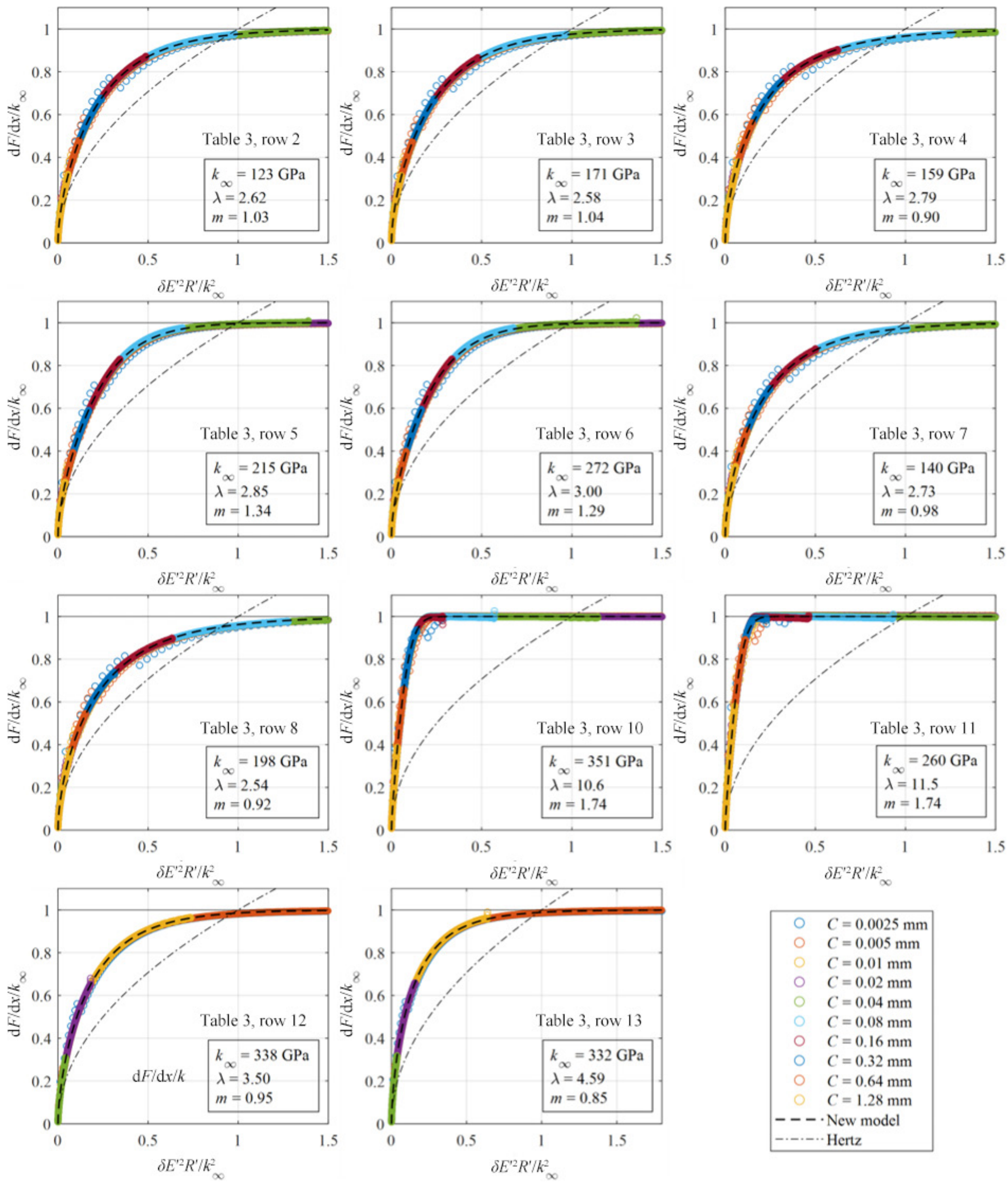


**Fig. A1** Normalized stiffness vs. normalized displacement $\delta'$. Comparison between FEM, Eq. (17) and Hertz's theory. Data from Table 3, rows 2, 3, 4, 5, 6, 7, 8, 10, 11, 12, and 13.

$$\frac{\partial F}{\partial \delta} = k_\infty \left(1 - \frac{1}{\sqrt{\delta'} + e^{\lambda x}}\right) \tag{B8}$$

Note: Eq. (B8) is obtained from Eq. (B2) with $g = e^{\lambda\delta'} - 1$. Not accurate enough.

Functions with three parameters $(k_\infty, \lambda_1, \lambda_2)$:

$$\frac{\partial F}{\partial \delta} = k_\infty \left[1 - \left(1 - \frac{1}{\sqrt{\lambda_2}}\right) e^{-\lambda_1 \delta'}\right] \left(1 - e^{-\lambda_2 \delta'}\right)^{\frac{1}{2}} \tag{B9}$$

Note: Eq. (B9) is obtained from Eq. (B2) with $g_1 = \left[(1 - e^{-\lambda_2 x'})/\lambda_2\right]^{\frac{1}{2}}$, $g_2 = \left(1 - e^{-\lambda_2 x'}\right)^{\frac{1}{2}}$, and $g_3 = e^{-\lambda_1 x}$. Good accuracy. Two local minima may exist for $\lambda_1$ and $\lambda_2$ giving discontinuous functions for the parameters estimation, which is an undesirable feature.

Functions with three parameters $(k_\infty, \lambda, m)$:

$$\frac{\partial F}{\partial \delta} = k_\infty \left[1 - e^{-\left(\sqrt{\delta'^m} - (\lambda\delta')^m\right)}\right] \tag{B10}$$

Note: Eq. (B10) is an ad hoc modification of Eq. (B5), adding $m$. It has a single local minimum for the parameters, which is a desirable feature. It has the best accuracy amongst the three-parameter functions tested.

Functions with 5 parameters $(k_\infty, \lambda_1, \lambda_2, \lambda_3, \lambda_4)$:

$$\frac{\partial F}{\partial \delta} = k_\infty \left[1 - \left(1 - \frac{1}{\sqrt{\lambda_2}}\right) \mathrm{e}^{-\left(\lambda_1 \delta'\right)^{\lambda_3}}\right] \left(1 - \mathrm{e}^{-\left(\lambda_2 \delta'\right)^{\lambda_4}}\right)^{\frac{1}{2\lambda_4}} \quad \text{(B11)}$$

Note: Eq. (B11) is an ad hoc modification of Eq. (B9), adding $\lambda_3, \lambda_4$. The accuracy is improved. It has too many free parameters, and therefore it is impractical.

Other similar variations of the functions above were also tested, but they are not reported for brevity.

## Acknowledgements

The authors acknowledge the joint financial support of Alberto Betti's PON Research and Innovation 2014–2020 Ph.D. Scholarship by the Italian Ministry of University and Research and Nuovo Pignone Tecnologie s.r.l. of the Baker Hughes Company Group.

## Declaration of competing interest

The authors have no competing interests to declare that are relevant to the content of this article. The author Enrico Ciulli is the Editorial Board Member of this journal.

## References

[1] Hertz H. Ueber die Berührung fester elastischer Körper. *J Reine Angew Math* **1882**(92): 156–171 (1882)

[2] Johnson K L. One hundred years of hertz contact. *P I Mech Eng* **196**(1): 363–378 (1982)

[3] Greenwood J A, Tripp J H. The contact of two nominally flat rough surfaces. *P I Mech Eng* **185**(1): 625–633 (1970)

[4] Johnson K, Kendall K, Roberts A D. Surface energy and the contact of elastic solids. *P R Soc A* **324**: 301–313 (1971)

[5] Tian Q, Flores P, Lankarani H M. A comprehensive survey of the analytical, numerical and experimental methodologies for dynamics of multibody mechanical systems with clearance or imperfect joints. *Mech Mach Theory* **122**: 1–57 (2018)

[6] Bartel D L, Burstein A H, Toda M D, Edwards D L. The effect of conformity and plastic thickness on contact stresses in metal-backed plastic implants. *J Biomech Eng* **107**(3): 193–199 (1985)

[7] Germaneau A, Peyruseigt F, Mistou S, Doumalin P, Dupré J C. 3D mechanical analysis of aeronautical plain bearings: Validation of a finite element model from measurement of displacement fields by digital volume correlation and optical scanning tomography. *Opt Laser Eng* **48**(6): 676–683 (2010)

[8] He W, Chen Y, He J C, Xiong W L, Tang T, Ouyang H. Spherical contact mechanical analysis of roller cone drill bits journal bearing. *Petroleum* **2**(2): 208–214 (2016)

[9] Ciulli E, Forte P, Antonelli F, Minelli R, Panara D. Tilting pad journal bearing ball and socket Pivots: Experimental determination of stiffness. *Machines* **10**(2): 81 (2022)

[10] Perrson A. On the stress distribution of cylindrical elastic bodies in contact. Ph.D. Thesis. Gothenburg (Sweden): Chalmers University of Technology, 1964.

[11] Popov V L, Heß M, Willert E. Normal contact without adhesion. In: *Handbook of Contact Mechanics*. Berlin (Germany): Springer, 2019: 5–66.

[12] Goodman L E, Keer L M. The contact stress problem for an elastic sphere indenting an elastic cavity. *Int J Solids Struct* **1**(4): 407–415 (1965)

[13] Fagan M J, McConnachie J. A review and detailed examination of non-layered conformal contact by finite element analysis. *J Strain Anal Eng* **36**(2): 177–195 (2001)

[14] Askari E, Andersen M S. A closed-form formulation for the conformal articulation of metal-on-polyethylene hip prostheses: Contact mechanics and sliding distance. *P I Mech Eng H* **232**(12): 1196–1208 (2018).

[15] Zhang J, Guo H W, Liu R Q, Deng Z Q. Nonlinear characteristic of spherical joints with clearance. *J Aerosp Technol Manag* **7**(2): 179–184 (2015)

[16] Liu C S, Zhang K, Yang L. Normal force-displacement relationship of spherical joints with clearances. *J Comput Nonlin Dyn* **1**(2): 160–167 (2006)

[17] Pérez-González A, Fenollosa-Esteve C, Sancho-Bru J L, Sánchez-Marín F T, Vergara M, Rodríguez-Cervantes P J. A modified elastic foundation contact model for application in 3D models of the prosthetic knee. *Med Eng Phys* **30**(3): 387–398 (2008)

[18] Heß M, Forsbach F. An analytical model for almost conformal spherical contact problems: Application to total hip arthroplasty with UHMWPE liner. *Appl Sci* **11**(23): 11170 (2021)

[19] Jia Y H, Chen X L. Application of a new conformal contact force model to nonlinear dynamic behavior analysis of parallel robot with spherical clearance joints. *Nonlinear Dynam* **108**(3): 2161–2191 (2022)

[20] Tudor A, Laurian T, Popescu V M. The effect of clearance and wear on the contact pressure of metal on polyethylene hip prostheses. *Tribol Int* **63**: 158–168 (2013)

[21] Kalker J J. Survey of wheel: Rail rolling contact theory. *Vehicle Syst Dyn* **8**(4): 317–358 (1979)

[22] Blanco-Lorenzo J, Santamaria J, Vadillo E G, Correa N. On the influence of conformity on wheel–rail rolling contact mechanics. *Tribol Int* **103**: 647–667 (2016)

[23] Liu B B, Vollebregt E, Bruni S. Review of conformal wheel/rail contact modelling approaches: Towards the application in rail vehicle dynamics simulation. *Vehicle Syst Dyn* **62**(6): 1355–1379 (2024)

[24] Lee C H, Polycarpou A A. Assessment of elliptical conformal hertz analysis applied to constant velocity joints. *J Tribol* **132**(2): 024501 (2010)

[25] Sun Z G, Hao C Z. Conformal contact problems of ball-socket and ball. *Physcs Proc* **25**: 209–214 (2012)

[26] Fang X, Zhang C H, Chen X, Wang Y S, Tan Y Y. A new universal approximate model for conformal contact and non-conformal contact of spherical surfaces. *Acta Mech* **226**(6): 1657–1672 (2015)

[27] Fang X, Zhang C H, Chen X, Wang Y S, Tan Y Y. Newly developed theoretical solution and numerical model for conformal contact pressure distribution and free-edge effect in spherical plain bearings. *Tribol Int* **84**: 48–60 (2015)

[28] Askari E. Mathematical models for characterizing non-Hertzian contacts. *Appl Math Model* **90**: 432–447 (2021)

[29] Yuan L, Bao H, Yao X F, Lu J G, Liu J. Distribution of conformal contact pressure in spherical plain bearings considering friction and free-edge effects. *P I Mech Eng J—J Eng* **235**(9): 1851–1867 (2021)

[30] Wu C N, Lin K H, Juang J Y. Hertzian load–displacement relation holds for spherical indentation on soft elastic solids undergoing large deformations. *Tribol Int* **97**: 71–76 (2016)

[31] Mitchell B, Yokoyama Y, Nassiri A, Tagawa Y, Korkolis Y P, Kinsey B L. An investigation of Hertzian contact in soft materials using photoelastic tomography. *J Mech Phys Solids* **171**: 105164 (2023)

[32] Childs D, Harris J. Static performance characteristics and rotordynamic coefficients for a four-pad ball-in-socket tilting pad journal bearing. *J Eng Gas Turb Power* **131**(6): 062502 (2009)

[33] Kirk R G, Reedy S W. Evaluation of pivot stiffness for typical tilting-pad journal bearing designs. *J Vib Acoust* **110**(2): 165–171 (1988)

[34] Ciulli E, Betti A, Forte P. The applicability of the hertzian formulas to point contacts of spheres and spherical caps. *Lubricants* **10**(10): 233 (2022)

[35] Hu J Q, Gao F H, Liu X M, Wei Y G. An elasto-plastic contact model for conformal contacts between cylinders. *P I Mech Eng J—J Eng* **234**(12): 1837–1845 (2020)

**Alberto Betti** is a Ph.D. student in the Industrial Engineering Program at the University of Pisa. In 2019 he got his B.Sc. degree in aerospace engineering with honors at the University of Pisa and in 2021 his M.Sc. degree in materials and nanotechnology with honors at the Scuola Normale Superiore of Pisa. His research interests include tribology, tilting pad journal bearings, and contact mechanics.

**Paola Forte** is a former associate professor of machine design, Ph.D. in tribology, at the University of Pisa. Her research activity has covered mainly rotor dynamics, gear dynamics and diagnostics, innovative automotive components and intelligent materials, and advanced aspects of lubrication. Her investigations have involved both numerical and experimental activities. She co-authored more than 200 scientific papers, 8 patents, and two didactical books on structural dynamics and machine design.

**Enrico Ciulli** is full professor of applied mechanics at the University of Pisa. His research activity covers principally tribological aspects as elastohydrodynamic and hydrodynamic lubrication, friction and wear problems, also under mixed and boundary lubrication conditions. He is involved in both basic studies and applications, particularly experimental investigations on gears and tilting pad journal bearings. He is author and co-author of more than 200 scientific papers and three didactical books on lubrication and mechanics.